remote sensing

MDPI

Article

The Role of Sea Surface Temperature Forcing in the Life-Cycle of Mediterranean Cyclones

Christos Stathopoulos, Platon Patlakas, Christos Tsalis and George Kallos *

School of Physics, National and Kapodistrian University of Athens, 15772 Athens, Greece; chrisstath@mg.uoa.gr (C.S.); platon@mg.uoa.gr (P.P.); ctsalis@mg.uoa.gr (C.T.)
* Correspondence: kallos@mg.uoa.gr

Received: 3 January 2020; Accepted: 24 February 2020; Published: 3 March 2020



Abstract: Air–sea interface processes are highly associated with the evolution and intensity of marine-developed storms. Specifically, in the Mediterranean Sea, the air–ocean temperature deviations have a profound role during the several stages of Mediterranean cyclonic events. Subsequently, this enhances the need for better knowledge and representation of the sea surface temperature (SST). In this work, an analysis of the impact and uncertainty of the SST from different well-known datasets on the life-cycle of Mediterranean cyclones is attempted. Daily SST from the Real Time Global SST (RTG_SST) and hourly SST fields from the Operational SST and Sea Ice Ocean Analysis (OSTIA) and the NEMO ocean circulation model are implemented in the RAMS/ICLAMS-WAM coupled modeling system. For the needs of the study, the Mediterranean cyclones Trixi, Numa, and Zorbas were selected. Numerical experiments covered all stages of their life-cycles (five to seven days). Model results have been analyzed in terms of storm tracks and intensities, cyclonic structural characteristics, and derived heat fluxes. Remote sensing data from the Integrated Multi-satellitE Retrievals (IMERG) for Global Precipitation Measurements (GPM), Blended Sea Winds, and JASON altimetry missions were employed for a qualitative and quantitative comparison of modeled results in precipitation, maximum surface wind speed, and wave height. Spatiotemporal deviations in the SST forcing rather than significant differences in the maximum/minimum SST values, seem to mainly contribute to the differences between the model results. Considerable deviations emerged in the resulting heat fluxes, while the most important differences were found in precipitation exhibiting spatial and intensity variations reaching 100 mm. The employment of widely used products is shown to result in different outcomes and this point should be taken into consideration in forecasting and early warning systems.

Keywords: Mediterranean cyclones; sea surface temperature (SST); RAMS model; WAM model; air-sea interface processes; SST forcing; sensitivity analysis

1. Introduction

Air–ocean interface processes are highly associated with the development, evolution, and intensity of extreme weather phenomena. Heat, moisture, and momentum exchanges due to ocean drag and thermodynamic disequilibrium between the ocean surface and the upper air result in intense atmospheric perturbations.

The Mediterranean Sea is an area where the aforementioned air–sea processes very often contribute to intense cyclonic activity. The presence of cold cut-off lows in the middle and upper troposphere blended with the warmer water surfaces leads to cyclogenesis. However, despite the considerable number of cyclones over the Mediterranean basin, only a few of them on an annual basis demonstrate characteristics similar to tropical cyclones (TCs), known as Mediterranean tropical-like cyclones (TLCs) or medicanes. Some important features characterizing a Mediterranean TLC in the literature are a

rounded shape with a cloudless core (cyclone eye), a drop in sea level pressure, a warm core structure at the mid-troposphere, heavy rainfall, and strong cyclonic winds [1–3].

Due to their formation in a marine environment, the air–ocean temperature deviations are one of the main triggering mechanisms of Mediterranean TLCs, equivalent to the tropical hurricanes [4–6]. The intrusions of cold air from the European mainland over the warmer sea surface enhance the role of the heat and moisture fluxes in the development and evolution of such systems.

The better knowledge and representation of sea surface temperatures (SSTs) during the several stages and the intensity of marine-developed storms have received significant attention in various associated studies. TCs have an impact on the upper-ocean layer causing alterations in the water surface temperature. Wind mixing and upwelling of colder water masses from deeper locations are some of the underlying processes taking place under TCs. This storm-induced SST cooling is expected to affect the air–sea enthalpy differences and the intensity of TCs [4], respectively.

An important limitation in numerical studies focusing on the sensitivity of the SST lies in the absence of large spatially distributed observational datasets. The sparsity of in-situ and satellite observations under extreme weather conditions [7] may lead to uncertainties both in the proper representation of the air–sea heat exchanges as well as the evaluation procedures. For example, in [4], a homogenous decrease of 3 °C in the SST fields during a Mediterranean cyclone led to a reduction in sea surface fluxes up to 150 W/m^2 and an elimination of the tropical characteristics. Moreover, in [8], the use of climatological SST in a modeling study of a Mediterranean cyclone decreased its lifetime. Towards the better description of the prevailing SST conditions, large data networks have been established in the last decade. This led to the construction of high-resolution SST gridded fields with the implementation of quality-controlled satellite, buoys and other ocean measurements [9,10].

Concurrently, the lack of information regarding the fast-evolving conditions in the air–water interface may conceal several features of these extreme events. To efficiently represent the on-going interplay between the atmospheric and oceanic environments, coupling methodologies have been developed [11]. Introducing the ocean effects in the operational European Centre Weather for Medium Range Weather Forecasting (ECMWF) high-resolution forecast improved the foresting intensity of hurricanes [12]. Likewise, the inclusion of air–ocean interaction methods in the Coupled Ocean/Atmosphere Mesoscale Prediction System for Tropical Cyclones (COAMPS-TC), enhanced the foresting capability in the track, the intensity, and the fine-scale structure in a number of hurricane cases [13].

In this context, this study aims at the understanding of how model results are affected in the simulation of Mediterranean cyclones using SSTs from different well-known datasets. More precisely, the current work examines the sensitivity of the atmospheric–ocean surface conditions on the formation and the evolution of Mediterranean TLCs. A coupled modeling system is used, consisting of atmospheric, wave, and ocean components. To consider the evolution of ocean temperature throughout the several stages of the cyclonic events, modeled and observational analysis SST fields enriched with various sources of remote sensing records are tested.

The manuscript is structured as follows. The modeling system used, the methodology followed, the description of the methodology, experimental cases, and the data used are described in Section 2. A brief analysis of the different input data used, the results of the performed experiments, and evaluation are discussed in Section 3. Further discussion and conclusions are presented in Section 4.

2. Model Description, Methodology, and Data Used

2.1. Atmospheric, Wave, and Ocean Components

A coupled modeling system was used to provide continuous feedback of information between the atmospheric–wave and ocean environments. The modeling system included an atmospheric and a wave model, online coupled. Moreover, the boundary conditions in the atmospheric model were continuously updated by a 2-D ocean component utilizing SST fields from several sources.

2.1.1. Atmospheric Component

The atmospheric component was an enhanced version of the Regional Atmospheric Modeling System (RAMS), the Integrated Community Limited Area Modeling System RAMS/ICLAMS [14–17]. Among its most notable characteristics is the online treatment of mineral dust and sea salt from wave breaking [18]. These natural aerosols contribute to model calculations through feedback mechanisms, including direct, semi-direct, and indirect effects in the radiation scheme [19] and the ice nuclei (IN) and cloud condensation nuclei (CCN) estimations [20].

2.1.2. Wave Component

The wave model used was the Wave Analysis Model (WAM) [21] version CY33R1 [22]. The model simulates the distribution of wave variance in different frequencies and propagation directions. The basic transport equation describes the evolution of the two-dimensional wave spectrum employed by the model. The solution of this equation leads to the calculation of different parameters, such as significant and swell wave height, peak frequency, and directional spread. The used version utilizes explicit source functions for the description of white-capping dissipation and bottom friction. Additional features, such as the calculation of depth induced wave breaking and shallow water effects, were also implemented.

2.1.3. Ocean Component

To consider the dynamic variation of the prevailing SST conditions, a 2-D model was constructed. This concerns an algorithm that inputs the SST from various sources and in the next step, interpolates it in a gridded domain corresponding to the spatial coverage of the atmospheric model. Unavoidably a small distortion of the initial SST fields is expected mainly in nearshore and complex areas due to the interpolation process.

2.1.4. Coupled Modeling System

For the model components to be able to operate synchronously in a coupled way, the OASIS-MCT [23] coupling module was used. The last allowed the exchange of parameters between the atmospheric–wave components in a two-way mode and the atmospheric–ocean in a one-way mode (Figure 1). The communication between the different components was performed in desired time intervals depending on its model time step. Surface wind speed components and air density were passed to the wave model, with wind speed to act as a forcing factor and density to be used in the computation of ocean surface stress. Simultaneously, the ocean surface roughness was transferred by the wave model to the atmospheric one. This allows a more realistic representation of the sea state conditions in the atmospheric model, affecting both the wind speed profile and the calculation of the surface heat fluxes. Precisely, the ocean surface roughness z_o was derived in the atmospheric model parameterized, employing wave characteristics, such as wave significant height (h_s) and wave slope (h_s/L_p), following the Taylor and Yelland parameterization [24]:

$$z_o = 1200 \cdot h_s \cdot (h_s/L_p)^{4.5} \quad (1)$$

with L_p the wavelength of the peak frequency. This relationship has been tested in a number of datasets and sea conditions, such as wind-sea, swell, and short/long fetch conditions [25–27].

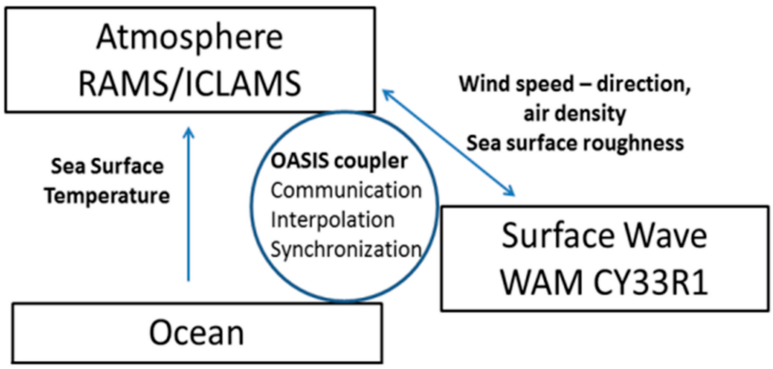


Figure 1. Model communication scheme.

2.2. Methodology and Data Used

For the needs of the study, three Mediterranean cyclones were simulated employing the coupled system and performing sensitivity tests with different SST fields. The analysis initially focused on the spatiotemporal evolution of the different ocean surface temperatures in terms of anomalies and comparison with data. Concerning the numerical experiments, an examination and comparison of storm tracks, maximum surface wind speed, and air–sea fluxes were performed, supported with available measurements. Furthermore, a phase analysis algorithm was applied for cyclone structure and characteristics based on the phase diagrams proposed by Hart [28]. A detailed description is given in Appendix A. Finally, the accumulated precipitation obtained from the different approaches was studied and assessed with the aid of remote sensing estimates.

2.2.1. Models Setup and Configuration

Concerning the atmospheric component, two nests were used, with the fine one to cover the entire Mediterranean and most parts of Europe and North Africa. This setup was followed to be able to capture the effects of the differential heating between Africa and Europe [29], the possible direct, indirect and semi-direct effects of dust particles and to include the whole Mediterranean Basin. The outer one was much larger to keep the lateral boundary conditions far from the area of interest. Subsequently, the wave model was running with a single domain covering the entire Mediterranean Sea (Figure 2). This configuration was expected to minimize the lateral boundary conditions problems and was computationally affordable.

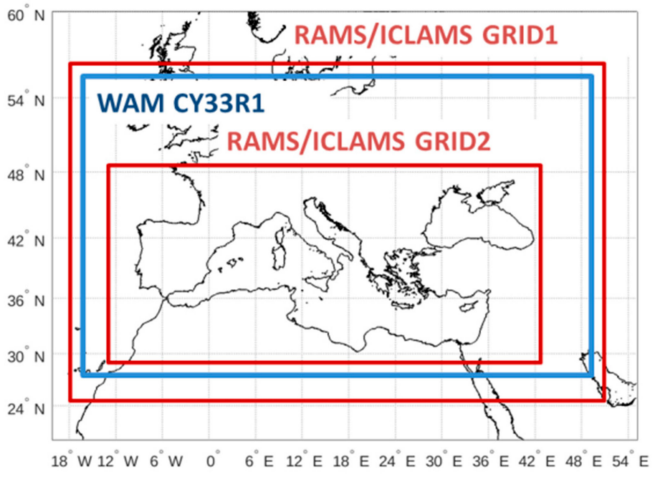


Figure 2. Model domains.

A more detailed description of the model configuration, including the lateral and boundary conditions, is summarized in Table 1.

Table 1. Model configuration.

RAMS/ICLAMS Model	
Nests	2
Resolution	18 km/6 km
Time step	15 sec/5 sec
Vertical Levels	42
Initial and lateral boundary conditions	National Centers for Environmental Prediction (NCEP) Final (FNL) Operational Global Analysis
Sea Surface Temperature (SST) gridded data	RTG daily (with a resolution of 0.083°) OSTIA hourly (with a resolution of 0.25°) NEMO hourly (with a resolution of 0.083°)
Soil texture and properties	Food and Agriculture Organization of the United Nations (FAO)
Elevation data	Shuttle Radar Topography Mission (SRTM)(3 arc-second resolution)
Vegetation and land cover	Olson Global Ecosystem categorization (30 arc-second resolution)
WAM Model	
Nests	1
Resolution	0.05°
Time step	30 sec
Number of frequencies	30
Number of wave directions	24
Bathymetry	ETOPO1 (1 minute resolution) from the National Centers for Environmental Information (NCEI) of the National Oceanic and Atmospheric Administration (NOAA).

The SST for the atmospheric model stem from three different sources briefly described below.

RTG-SST

The Real Time Global SST (RTG_SST) is a global operational analysis product available since 2001 [30]. An analysis algorithm operates once per day combining in-situ and satellite data of the last 24 h. In-situ data come from fixed buoys, drifting buoys, and ships. Satellite retrievals come from NOAA and METOP-A AVHRR data that are averaged in day and night fields following a physical algorithm. Currently, the RTG_SST data are provided on a daily basis on a resolution of 1/12 × 1/12 degrees.

OSTIA-SST

The Operational SST and Sea Ice Ocean Analysis (OSTIA), is a global coverage SST dataset produced at the United Kingdom Met Office [10] with a resolution of 1/4 × 1/4 degrees. The system blends in-situ data and satellite observations, a warm layer diurnal algorithm that assimilates the satellite data and a cool skin model. Remote sensing data of different coverage stem from eleven different sensors of Infrared and Microwave sensor type. Satellite retrievals come from SEVIRI, GOES-W, MTSAT 2, and METOP-A AVHRR data [31]. OSTIA SST analysis fields are used by the United Kingdom Met Office and European Centre Weather for Medium Range Weather Forecasting (ECMWF) models for operational forecasts.

NEMO–SST

Forecast SST data are available through the Operational Mercator global ocean analysis and forecast system. The system is based on the Nucleus for European Modeling of the Ocean (NEMO)

ocean model, version 3.1 [32], with a horizontal resolution of 1/12 × 1/12 degrees. Starting from the sea surface, fifty vertical levels are used up to 5000 m depth, with the first 28 distributing within the first 450 m water depth. Bathymetry data come from the GEBCO8 [33] database for depths less than 300 m and from ETOPO1 [34] for deeper waters. Model physics and recent updates and improvements concerning the advection, assimilation, and sea/ice schemes, as well as evaluation studies, can be found in [9,35].

2.2.2. Case Studies

Three recent Mediterranean cyclones with tropical-like characteristics were analyzed. The storm cases were selected from the EUMESTAT database, identified by an operating network of satellites. The events were generated and grew in a mature stage over the Central and Eastern Mediterranean waters. These areas belong to a zone where such systems usually appear during late autumn and early winter due to relatively high SST [36]. The selection was based on the availability of the OSTIA SST and the data for evaluation.

The selected cases and periods are summarized in Table 2. For the convenience of the reader, the performed simulations throughout the manuscript are stated with the names of the origin of the SST as RTG-sst, NEMO-sst, and OSTIA-sst.

Table 2. Cyclones and experimental periods.

Cyclone Name	Experimental Period
Trixi	26/10/2016 to 01/11/2016
Numa	15/11/2017 to 20/11/2017
Zorbas	27/09/2018 to 01/10/2018

The first Mediterranean storm took place during the period, 27 October to 1 November 2016. It was formed during the first hours of 27 October in the offshore area along the western shoreline of Italy. Moving southward, the system was located over relatively warm waters in the area east of Malta (Figure 3a), and from the first hours of 30 October (Figure 3b), an eye-like structure was developed and started moving eastward towards Greece. Afterward, the storm crossed the South Aegean Sea and rapidly lost its strength as it reached landfall on the southwest coast of Turkey during 1 November.

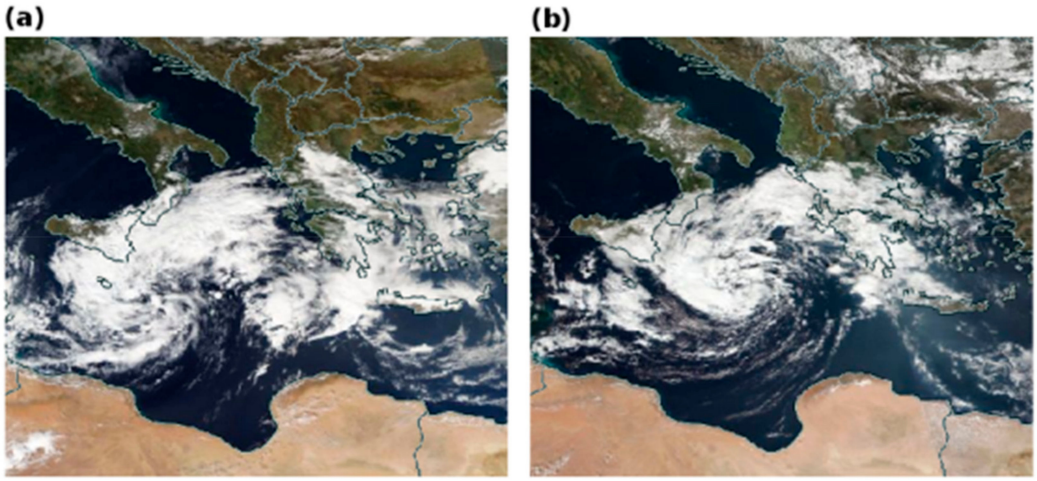


Figure 3. (**a**) Moderate Resolution Imaging Spectroradiometer (MODIS)/Aqua reflectance for 29 October 2016 and (**b**) Visible Infrared Imaging Radiometer Suite / National Polar-orbiting Partnership (VIIRS/NPP) Suomi reflectance for 30 October 2016.

The second Mediterranean cyclone under consideration occurred during November 2017. The cyclone was formed after the dissipation of an extra-tropical low that was located in the British Isles.

The storm moved southeastward and passed France and Italy on 15 November. The last hours of the same day, the storm started obtaining sub-tropical characteristics. During 17 November, when it was located in the Ionian Sea (Figure 4a), the storm presented tropical characteristics [37] that maintained until the next day (Figure 4b). Moving eastward on 19 November, it dissipated over the Greek Peninsula.

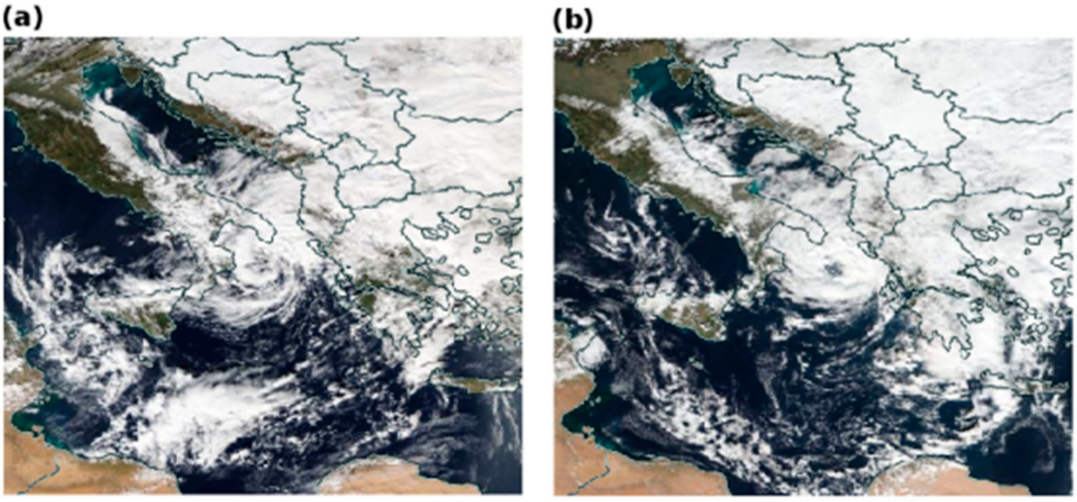


Figure 4. (**a**) MODIS/Aqua reflectance for 17 October 2017 and (**b**) VIIRS/NPP Suomi reflectance for 18 October 2017.

The third selected case was related to a storm developed over warm waters in the eastern Mediterranean Sea on 27 September 2018. Heading northeastward, the following day, the cyclone gradually intensified and obtained tropical-like characteristics (Figure 5a). The cyclone reached its peak as it approached the southwest part of Greece on 29 September (Figure 5b). Continuing northeastward, the storm passed along the Aegean Sea and dissipated over Turkey during the next day.

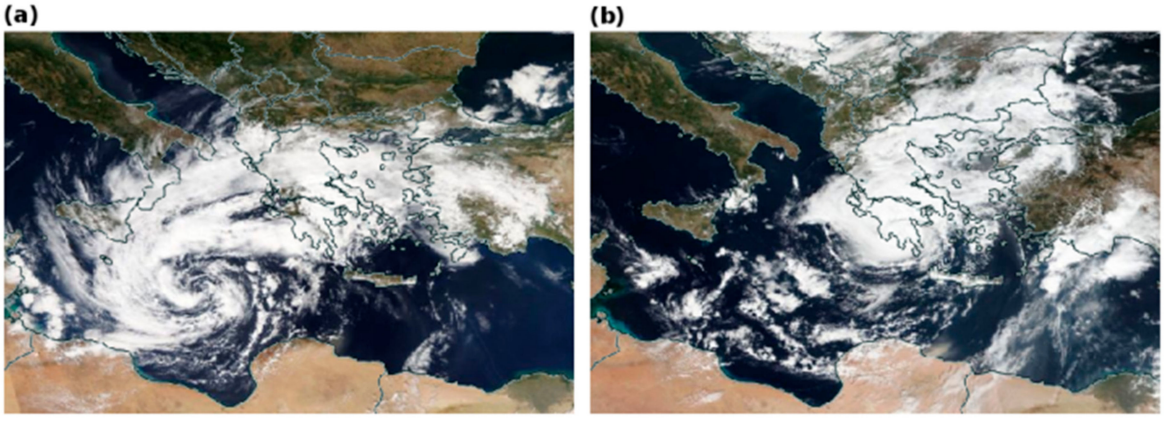


Figure 5. (**a**) MODIS/Aqua reflectance for 28 September 2018 and (**b**) VIIRS/NPP Suomi reflectance for 29 September 2018.

2.2.3. Data Used

For evaluation purposes, remote sensing, in-situ, and model reanalysis data were used. Satellite-based winds and precipitation were implemented from the Blended Sea Winds and the Integrated Multi-satellitE Retrievals for GPM (IMERG), respectively. Remotely sensed altimeter data from JASON2 and JASON3 satellite missions were employed for wave height comparison. Moreover, SST records from a buoy in the South Aegean Sea were used. To have an alternative estimate of the

derived heat fluxes and rainfall, Modern-Era Retrospective Analysis for Research and Applications, version 2 (MERRA-2) reanalysis data were also considered.

The Blended Sea Winds is a gridded and high-resolution dataset [38,39]. It contains surface wind speed and direction data on a global 0.25° grid in multiple time resolutions. Wind speed vectors are generated from multiple satellite observations stemming from the Defense Meteorological Satellites Program (DMSP) SSM/I, the QuikSCAT, the Advanced Microwave Scanning Radiometer–Earth Observing System (AMSR-E) and the Tropical Rainfall Measuring Mission (TRMM) Microwave Imager (TMI). A spatiotemporal interpolation is made to fill possible temporal and spatial gaps of the individual satellite samplings. At the same time, correction methods for the reduction in the subsampling aliases and the imported random errors are used. Concerning the wind direction, two sources are employed depending on the products. For research delayed mode product, the source is the National Centers for Environmental Prediction (NCEP) Reanalysis 2, while for the near-real-time product, the source is the numerical weather prediction of ECMWF. Nevertheless, data gaps are not completely eliminated and while the representation of wind fields is sufficient, errors in both low and high wind speed categories were found [40,41]. In this work, the finest temporal resolution of six-hours was implemented to test the model behavior regarding the cyclonic formulation and the maximum wind speed recorded.

IMERG is a precipitation product based on the inter-calibration, merging, and interpolation of measurements from a network of satellites together with microwave-calibrated infrared (IR) satellite estimates, precipitation gauge analyses, and potentially other precipitation estimators. More specifically, it utilizes TRMM and GPM eras globally. It has a spatial resolution of 0.1° × 0.1° and a temporal of 30 min covering up to ±60° latitudes. The system runs several times providing different products depending on user requirements. The first is a quick estimate (IMERG "early run"), provided with a 6-h delay for real-time applications, such as hazard predictions. The second provides better estimates as more data are taken into consideration. The so-called IMERG "late run", has a delay of 18 h and could be employed in other applications, such as crop forecasting. The final step is the one also used in the present study (IMERG "final run"). It uses monthly gauge data to create research-level products and comes at a 4-month delay. More details can be found in the following articles and references within [42–46]. It should be mentioned that several studies [47–49] have indicated an overestimation of IMERG products in the estimated precipitation under heavy rainfall events.

JASON2 and JASON3 altimetry missions perform global measurements of sea surface height [50,51]. Both repeat 256 passes in each cycle with an approximately 10 day return period. Wave height, altimetry range and other relevant data are measured at C (5.3 GHz) and Ku (13.575 GHz) band frequencies. For the needs of the study, significant wave records from the Ku band frequency were used after a simple quality control procedure for the removal of erroneous data.

Modern-Era Retrospective Analysis for Research and Applications, version 2 (MERRA-2), is a global atmospheric reanalysis with a resolution of 0.5° × 0.625° degrees [52]. Among its capabilities is the assimilation of satellite measurements and aerosol observations and new schemes for mass conservation and water balance in forecasting and assimilation procedures [53].

3. Results and Discussion

The study examined the uncertainty in model results using different SSTs in the simulation of Mediterranean cyclones. As a first step, a comparison between the time-series of the SST from the three selected datasets and an independent source that was data from a buoy with reference 61277 at a selected location was performed. The location corresponded to the coordinates (35.72° N, 25.13° E), , that was inside the affected zone of the selected events. Unfortunately, no other buoy covering all selected cases was available. Regarding the case of cyclone Trixi, SSTs from RTG and NEMO compared quite well, following the fluctuations of the observational data (Figure 6a). The SST from OSTIA tended to underestimate at this point, providing values around 21.0–21.5 °C, about one degree less than the other sources. The second case concerning cyclone Numa took place during November with lower temperatures as expected (Figure 6b). The NEMO and OSTIA products underestimated the values

to a small degree, while RTG could be characterized by a slight overestimation. In any case, the first two datasets followed the trend of the measurements, while RTG did not. For the case of cyclone Zorbas, the sea was warmer than in the previous case since it was October (Figure 6c). NEMO and OSTIA datasets had a similar behavior as compared with the observations with values that gradually decreased. The RTG performance could be separated into two parts. During the first two days, RTG overestimated the water temperature, while for the rest of the duration of the event, it managed to better capture the SST. It should be noted that RTG is a daily product, something easily understood through the figures.

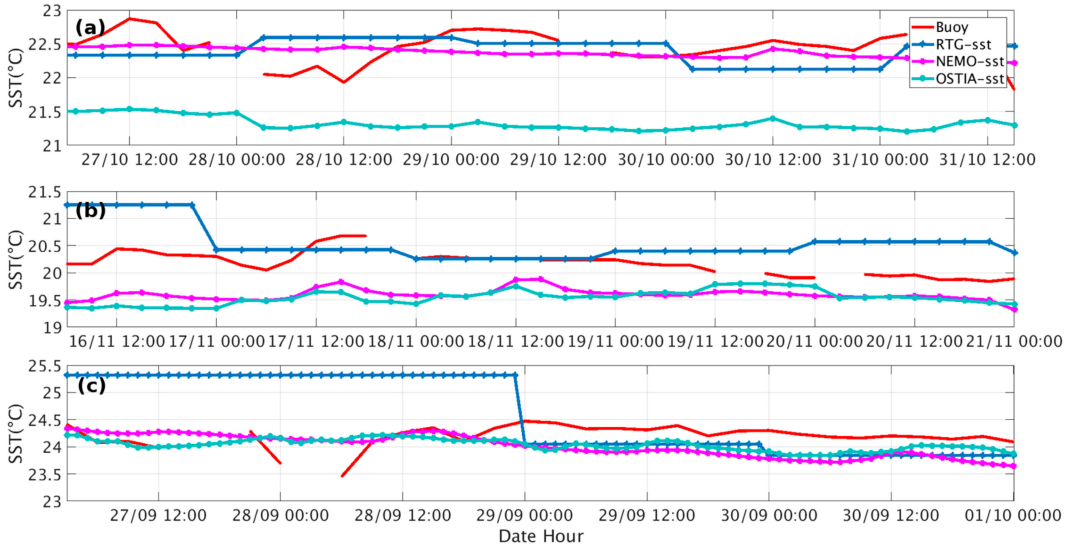


Figure 6. RTG, NEMO, OSTIA and recorded SST evolution at a selected location of the 61277 buoy during (**a**) cyclone Trixi (2016), (**b**) cyclone Numa (2017), and (**c**) cyclone Zorbas (2018).

The spatial variability of the SST alongside the different phases of the events under investigation is also discussed. Precisely, the differences between the SST in several stages of the simulations and the initial one were examined (Figure 7). For simplicity, the SST anomalies for the case of cyclone Zorbas are the ones illustrated. This event was also found to present the highest variations in the evolution of water surface temperatures between the various datasets. In all cases, sea surface tended to get colder as the system evolved. This is something expected as the cyclone gains energy from the warm water. Other processes contributing to SST reduction can be evaporative cooling processes, mixing of the top water layers due to wind and precipitation effect. It is well known that tropical cyclones can impact the upper ocean by causing SST cooling by as much as 6 °C [54]. In general, SST cooling can decrease the air–sea heat exchange and, therefore, reduce cyclone intensity [55–57]. Obviously, here, the cooling effects were smaller due to the scaling of the event and the local characteristics of the basin. Beginning with the first 24 h of the simulations, the largest differences were observed in the NEMO product with the SST dropping more than one degree in the area north of the cyclonic center. For the same time, the OSTIA dataset that is satellite oriented was characterized by a slight maximum drop around 0.5 °C. In contrast, the RTG daily differences seemed to be negligible. It should also be mentioned that the initial fields of RTG and NEMO showed a similar pattern and magnitude, while the OSTIA had slightly lower values in the initial fields. Continuing with the next 48 h, the maximum temperature drop of 2 °C was observed in NEMO-sst simulation, while both RTG and OSTIA had a maximum decrease of around 1 °C. Concurrently in RTG, this decrease was traced on the east side of the storm, while for the other two datasets, it was around the cyclone. Finally, the third day, 72 h from the beginning of the simulations, was characterized by even lower temperatures. The passage of the cyclone deepened the thermocline base, causing a further cooling of the ocean surface temperature. The maximum differences were also found in the NEMO-sst output, followed by RTG and OSTIA.

Here the cyclone was in its dissipation phase, and the cooling was due to processes that took place earlier this day, such as wind mixing and upwelling.

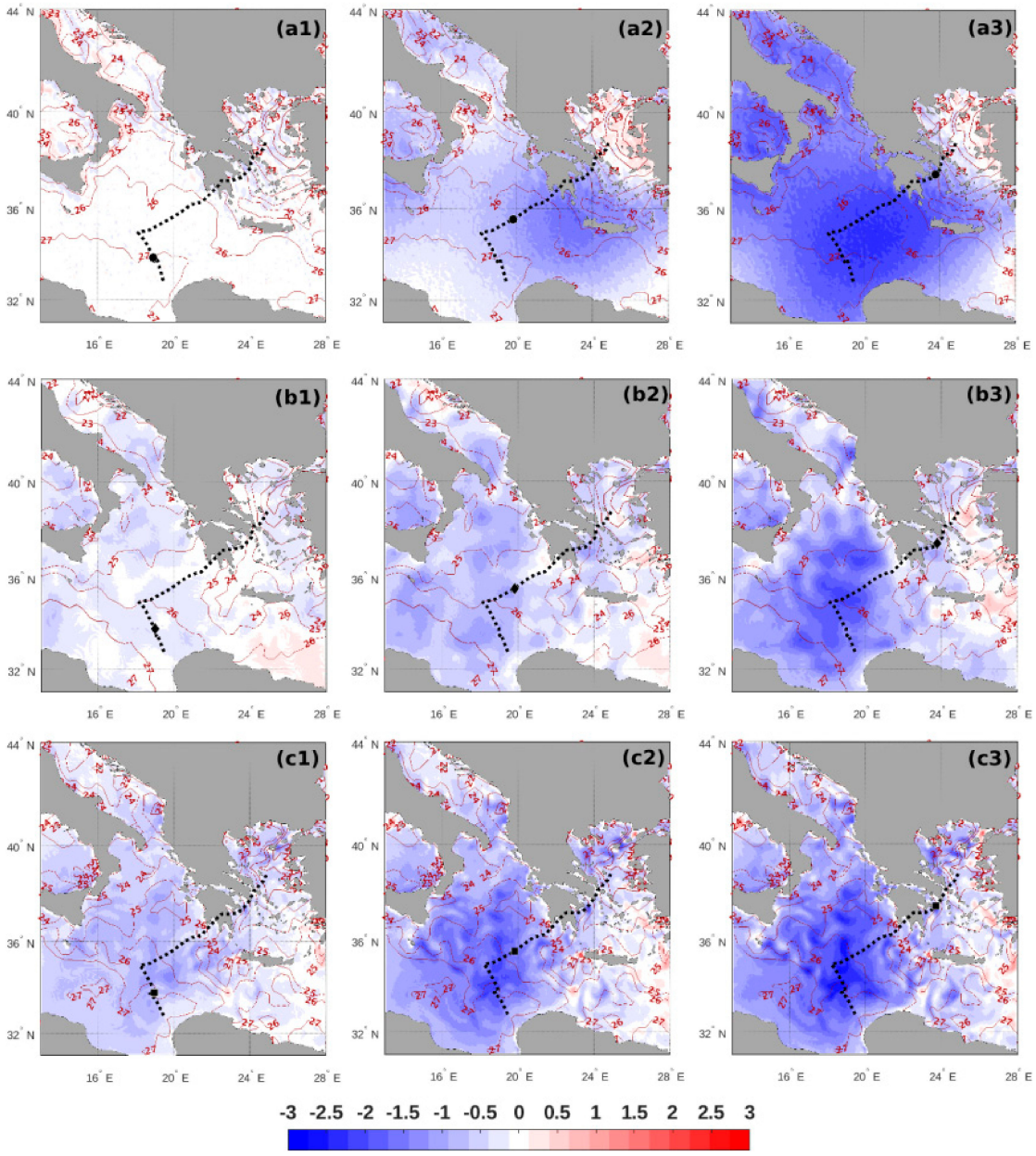


Figure 7. Differences in SST (in °C) spatial distribution between the 24 h, 48 h, and 72 h ahead and the initial field at 27 September 2019 at 00:00 UTC given in contour lines during cyclone Zorbas for (**a1**–**3**) RTG-sst, (**b1**–**3**) OSTIA-sst, and (**c1**–**3**) NEMO-sst. Lines indicate storm tracks and mark the position of the lower mean sea level pressure (MSLP) 24 h, 48 h, and 72 h ahead from 27 September 2019 at 00:00 UTC.

Model results in storm tracks and intensities based on surface pressure and particularly the mean sea level pressure (MSLP), are illustrated in Figure 8. Overall, small differences between the path and the translation speed appeared. This can also be explained due to the dependence of the cyclone tracks on large-scale processes. Spatially, divergences could be mainly traced in the initial stage of the storms, while differences during their lifetime emerged only in the 2016 storm (Figure 8a). Concerning the evolution of MSLP in time, a consistency in the variation of the minimum values between the different

numerical experiments was presented. Regarding the intensity, notable deviations appeared in cyclone Trixi and Zorbas cases. In cyclone Trixi, the numerical simulation of NEMO-sst provided the lowest MSLP values, while in cyclone Zorbas, the use of RTG SST distinctly increased the strength of the cyclone with a drop of 1 hPa as compared to the other two simulations.

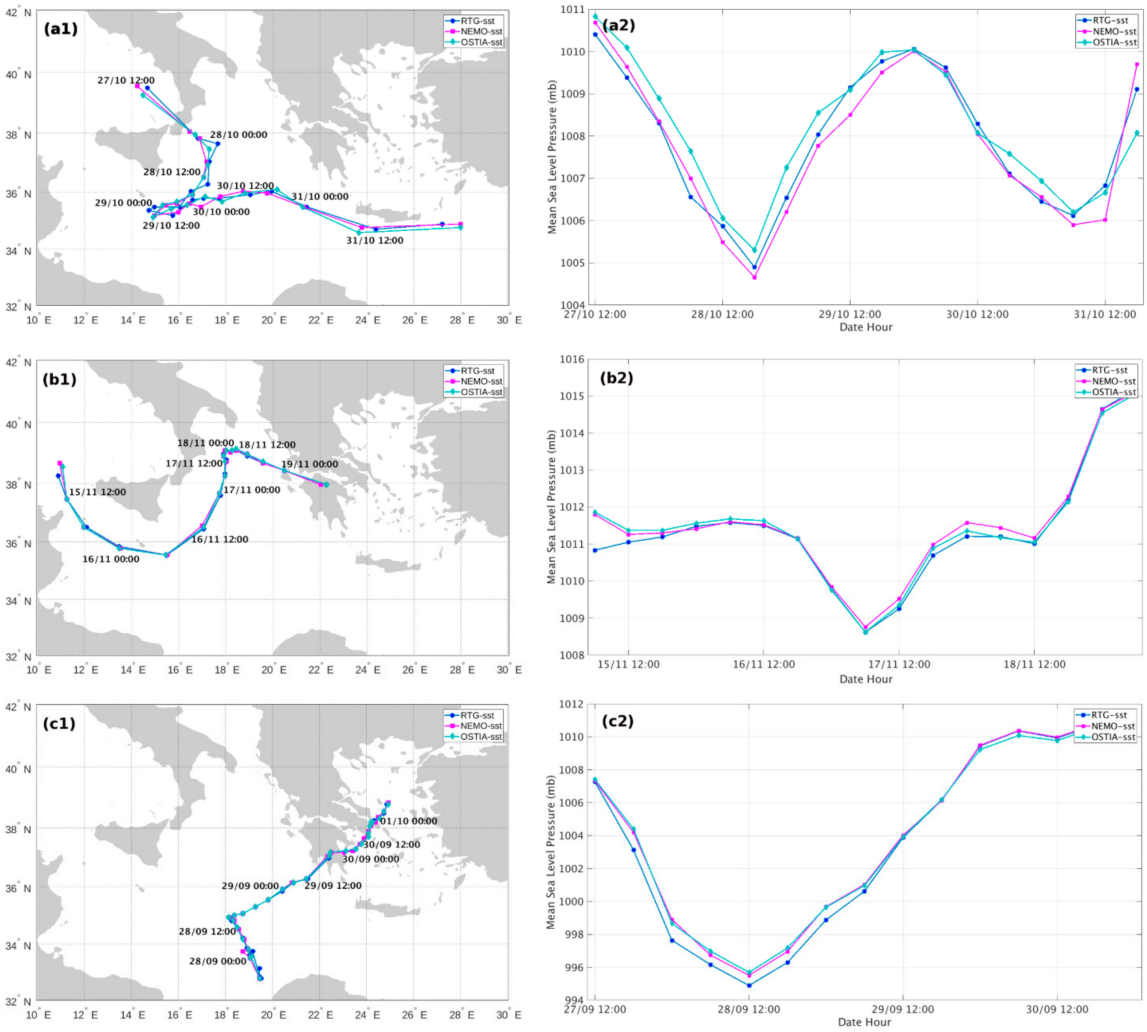


Figure 8. Storm tracks from RTG-sst, NEMO-sst, and OSTIA-sst simulations represented by the MSLP in six-hour intervals and MSLP evolution for (**a1**–**2**) cyclone Trixi, (**b1**–**2**) cyclone Numa, and (**c1**–**2**) cyclone Zorbas.

To understand the tropical development during the cyclonic evolution along with the level of the warm/cold core structure and symmetry, cyclone phase diagrams have been formed for each case. Precisely, the daily structural behavior for each cyclone is illustrated. Both parameters of thermal symmetry and thermal winds were calculated in a radius of 200 km around the location of MSLP for six-hour intervals.

Cyclone Trixi presented a symmetric formation for most of its lifetime, with a weak warm-core structure in the lower troposphere and cold-core in the upper, as displayed in Figure 9. A transition from extra-tropical to tropical behavior is illustrated for the 28 October at 12:00, where the minimum surface pressure appeared. The period before and after, the storm exhibited extra-tropical characteristics.

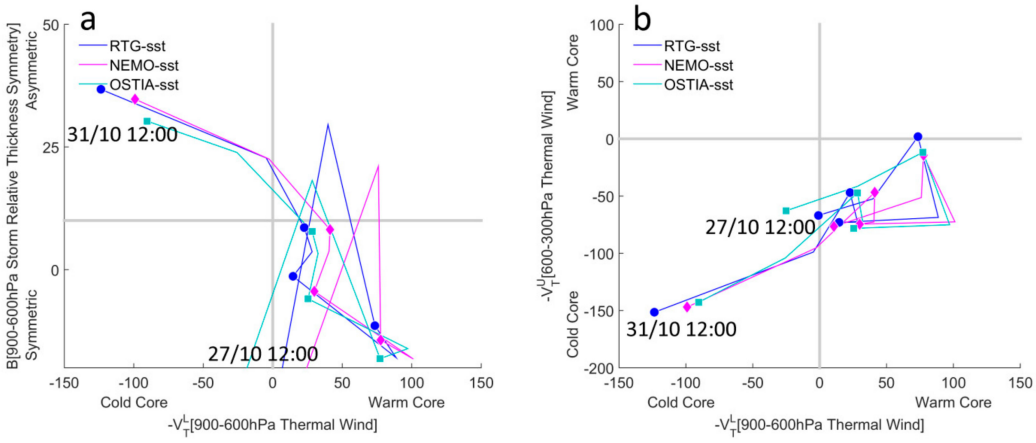


Figure 9. Phase space diagrams of (**a**) $-V_T^L$ vs. B for 900–600 hPa evolution and (**b**) $-V_T^L$ (900–600 hPa) vs. $-V_T^U$ (600–300 hPa) evolution from RTG-sst, NEMO-sst, and OSTIA-sst simulations during cyclone Trixi. Markers are shown every 12:00 UTC.

Cyclone Numa also demonstrated extra-tropical type characteristics. The system underwent two different phases, as shown in Figure 10. In the first, starting from 16 November, a warm-core structure emerged in the lower atmospheric layers that lasted for three days. This period the cyclone also tended to be symmetric for less than twelve hours. During the second phase from 19 November, the cyclone obtained an asymmetric cold-core structure.

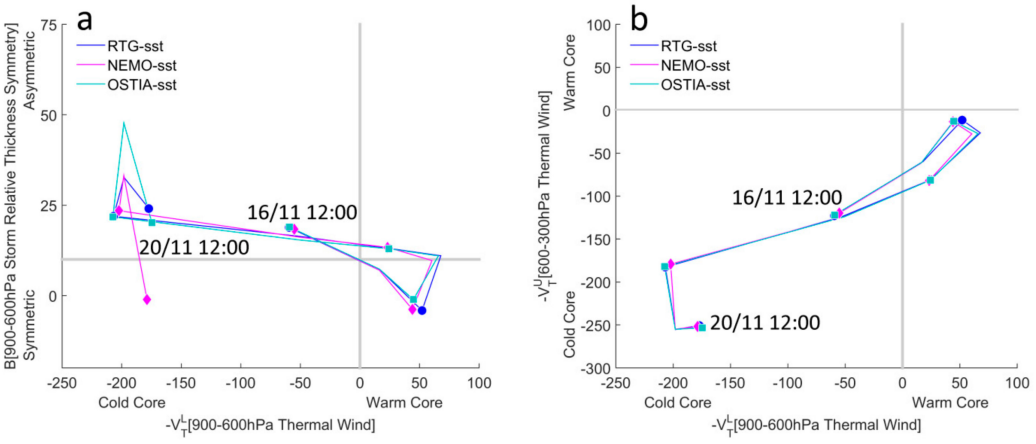


Figure 10. Phase space diagrams of (**a**) $-V_T^L$ vs. B for 900–600 hPa evolution and (**b**) $-V_T^L$ (900–600 hPa) vs. $-V_T^U$ (600–300 hPa) evolution from RTG-sst, NEMO-sst, and OSTIA-sst simulations during cyclone Numa. Markers are shown every 12:00 UTC.

Cyclone Zorbas rapidly evolved to a tropical cyclone twelve hours after its genesis on 27 September with a deep warm-core structure (Figure 11). A thermally direct circulation was evident in both the lower and upper troposphere, which lasted until 29 September at 18.00. Reaching the Greek Peninsula the next hours, the system weakened and obtained an asymmetric structure.

Based on the phase diagram analysis, more intensified warm-core characteristics were illustrated in cyclone Trixi and Zorbas simulations using the RTG SST dataset (Figures 9b and 11b). Apart from this point, no significant differences could be traced in the structural features from the implementation of different SSTs.

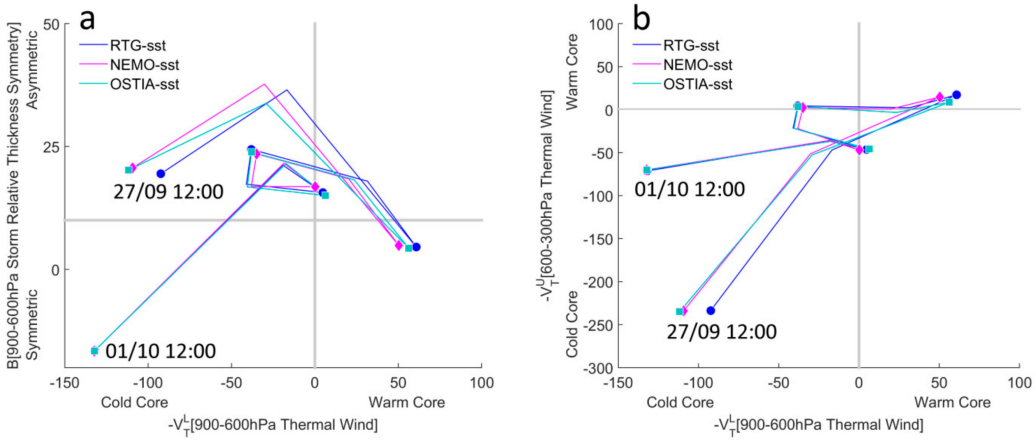


Figure 11. Phase space diagrams of (**a**) $-V_T^L$ vs. B for 900–600 hPa evolution and (**b**) $-V_T^L$ (900–600 hPa) vs. $-V_T^{UI}$ (600–300 hPa) evolution from RTG-sst, NEMO-sst, and OSTIA-sst simulations during cyclone Zorbas. Markers are shown every 12:00 UTC.

The coupling of ocean surface temperature in the atmospheric–wave environment can also be expressed in terms of air–sea fluxes. It should also be stated that air–sea temperature and humidity differences are not the only source of upward/downward energy transfer in the marine boundary layer. Wind stress and ocean surface roughness also have an impact on momentum, heat, and moisture fluxes. Both were also considered in the implemented atmospheric–wave/ocean modeling system. The maximum interfacial air–sea sensible and latent heat fluxes were estimated from the different SST used in the model simulations (Figure 12). The heat fluxes from MERRA-2 reanalysis were also demonstrated to have an additional individual dataset for reference. Maximum values were based on the storm tracks of the surface pressure, where the sensible and latent heat maxima which emerged over water in a radius of 5° around the center of the cyclone were taken into account. Latent heat fluxes clearly overcame the sensible heat. The highest energy fluxes appeared in cyclone Zorbas's case due to warmer water temperatures prevailing in the area where the cyclone was generated. Overall, the intensity in fluxes was higher in RTG-sst simulations. This can also be related to the absence of SST cooling in RTG included in diurnal variability. Differences between the simulations were mainly traced in cyclone Trixi and secondly in cyclone Zorbas. In contrast, the resulting fluxes in cyclone Numa were characterized by smaller deviations between the different approaches. For cyclone Trixi, the peaks in the maximum sensible heat fluxes were almost the same for all the simulations. The highest values presented for the RTG-sst simulations exceeded the other two simulations in a range of 50 to 70 W/m^2. Concerning the maximum latent heat fluxes, again, the fluxes from RTG simulations in most of the cases were higher than those from the other two simulations in most of the cyclonic lifetimes. In this case, differences reached 150–200 W/m^2. The same tendency, but for smaller time scales, was illustrated in cyclone Zorbas. The heat fluxes stemming from RTG-sst simulations exceeded the ones from NEMO-sst and OSTIA-sst simulations. Precisely, the differences were up to 50 W/m^2 for the sensible and between 100 to 200 W/m^2 for the latent heat fluxes. For almost all cases, heat fluxes from MERRA-2 fluctuated in a similar manner to the ones from the performed simulations. Certainly, the variation of the maximum fluxes was traced in lower energy scales due to the coarser resolution of MERRA-2. Even though there were still some cases where heat fluxes values of MERRA-2 could be found close to the fluxes from the model simulations.

To further analyze the differences between the applied methods, the temporal development of maximum surface wind speed was examined. In this case, wind speed magnitudes from blended sea winds were also used (Figure 13). It should be noted that blended winds were employed as an indicator for the variation and tendency of the forecasted winds rather than a means for evaluation, due to the issues stated earlier in the description of the Blended Sea Winds product. Considering that wind speed and pressure are associated parameters through the pressure gradients, maximum wind

speed also deviated similarly to the lowest pressure values for the different SST couplings. For all cases, wind speed compared well to the one presented by the Blended Sea Winds. Differences in the maximum values were evident in the range of 4 to 5 m/s and could be found in the cyclones Trixi and Zorbas. It should also be stated that maximum wind speed results in cyclone Numa are in good agreement with the ones presented in a similar study for the same event [37].

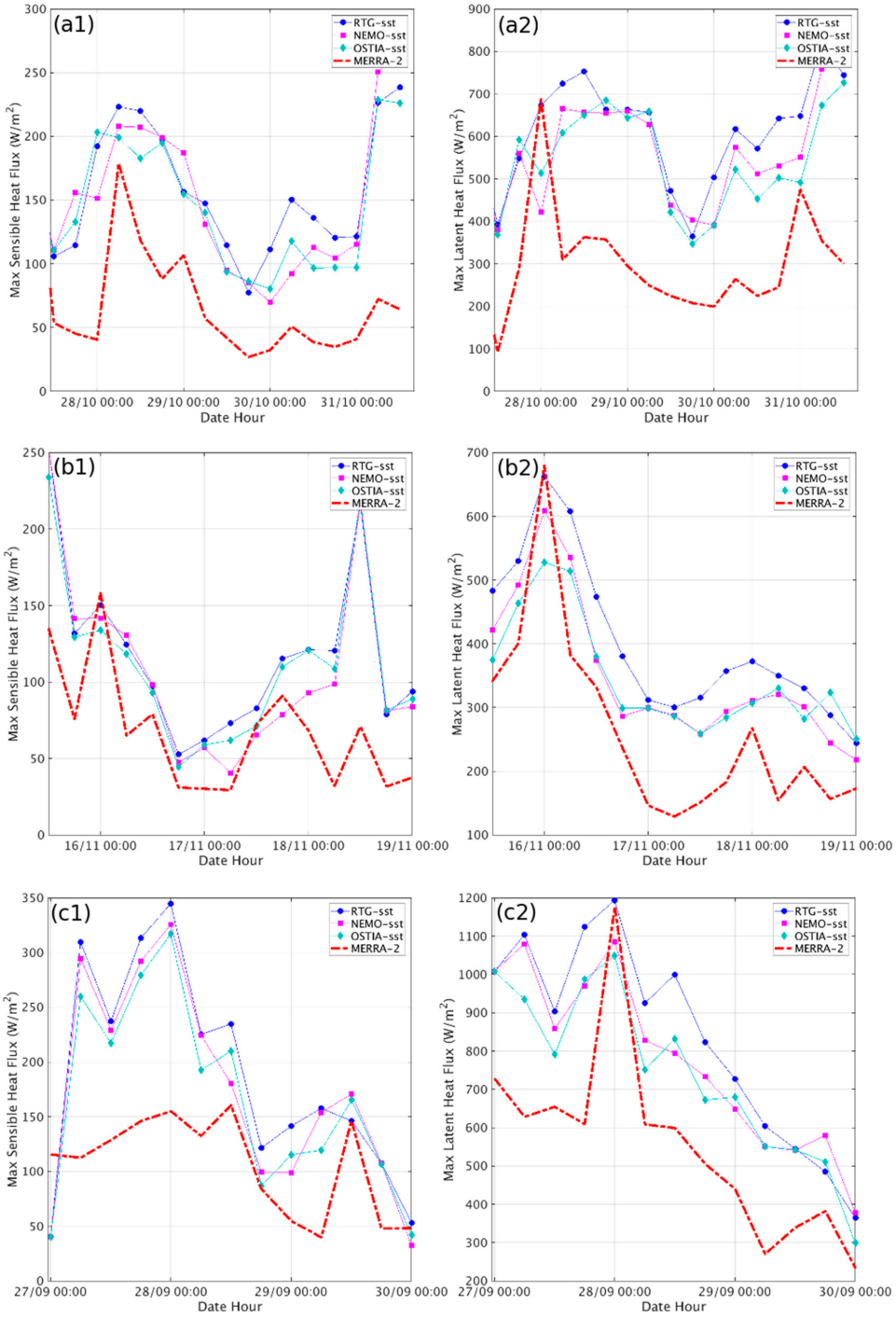


Figure 12. Maximum sensible heat and latent heat fluxes from RTG-sst, NEMO-sst, and OSTIA-sst simulation and MERRA-2 reanalysis in six-hour intervals during (**a1**–**2**) cyclone Trixi, (**b1**–**2**) cyclone Numa, and (**c1**–**2**) cyclone Zorbas.

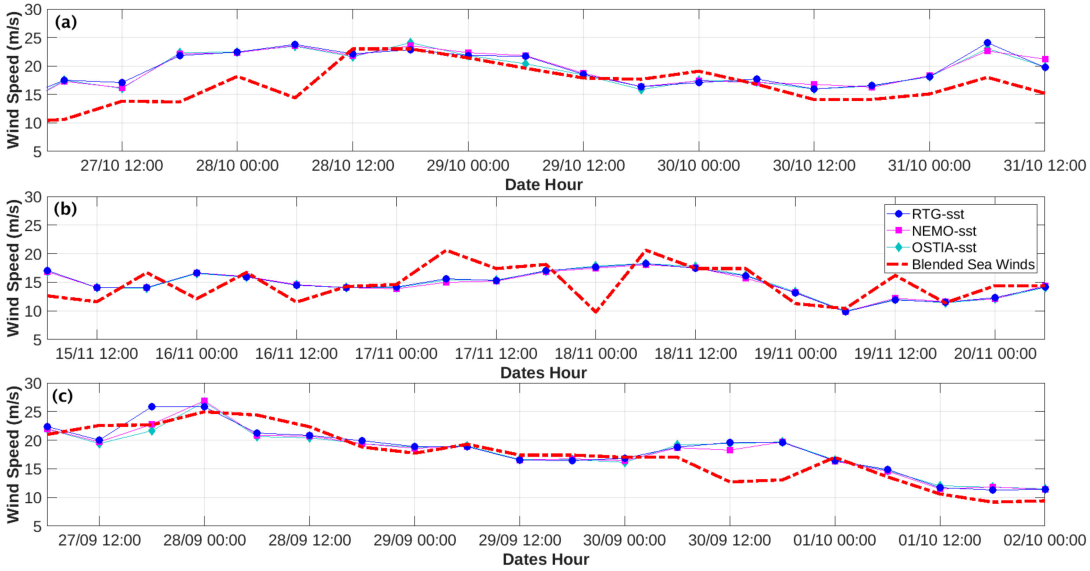


Figure 13. Maximum surface wind speed evolution from RTG-sst, NEMO-sst, and OSTIA-sst simulations and Blended Sea Winds during (**a**) cyclone Trixi, (**b**) cyclone Numa, and (**c**) cyclone Zorbas.

The resulting significant wave heights from the different runs were evaluated against the ones derived from JASON satellites. To perform the comparison, satellite data from the nearest hourly model time were employed. Figure 14 displays the cumulative scatter plots for each applied methodology covering the significant wave height (SWH) values from all the test cases among the results in statistical indicators of performance. Particularly, the bias (in m), the mean absolute error (MAE) (in m), the root mean square error (RMSE) and the Pierson correlation coefficient (Corr.Coef) were used [58]. For all cases, SWHs seemed to be gathered in the range of 0 to 2.5 m, while statistical results were almost identical. This was rather expected based on the aforementioned results in wind speed. Distances (errors) between observed and model values were increasing for higher SWHs with a tendency for over-prediction for waves over approximately 5 m.

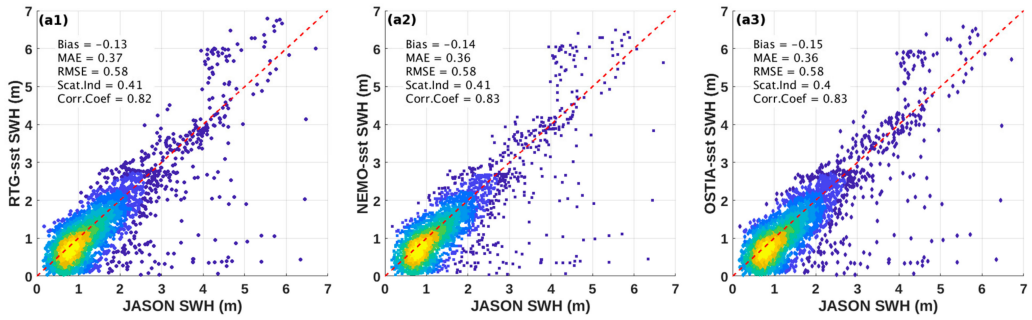


Figure 14. Density scatter plots between modeled and JASON (satellite) significant wave heights for (**a1**) RTG-sst, (**a2**) NEMO-sst and (**a3**) OSTIA-sst simulations, gathering all experimental cases.

To examine the effects in precipitation, the spatial and temporal distributions of modeled and satellite estimated rainfalls from IMERG were compared. The purpose was to identify qualitatively whether the rain patterns and locations of the maxima between modeled and satellite estimates were in agreement. Therefore, the comparison concerned the accumulated precipitation fields in the modeling of each cyclone. Accumulated precipitations from MERRA-2 were also considered. To better compare the rain fields from the different simulations, RTG-sst simulations were used as a reference and subtracted from NEMO-sst and OSTIA-sst simulations.

For cyclone Trixi, both satellite and modeled accumulated rains were concentrated in the western region of Greece in the south Ionian Sea, as shown in Figure 15. The spatial differences between RTG-sst–OSTIA-sst and RTG-sst–NEMO-sst indicated that all modeled precipitation fields were positioned in the same area. The same pattern could be observed and for the MERRA-2 precipitation fields. A close agreement in the distribution, as well as the position of the maxima between RTG-sst modeled and IMERG satellite data, was evident. A notable underestimation with regard to the remote sensing rain data occurred in the peak values. This can be partially attributed to the resolution of the model, the forcing input, the cloud microphysical scheme used and to the fact that IMERG data tend to overestimate precipitation in extreme conditions. OSTIA-sst rainfall fields had a different spatial distribution, as compared to those of RTG-sst and could overall be characterized as slightly lower. This was due to the changes in the path of the cyclone and the differences in the distribution and magnitude of the SST fields. However, the same point was not presented in RTG-sst–NEMO-sst comparison, where a spatial shift of around 100 mm in the maximum values appeared. These were positively correlated to the deepening of the cyclone in this simulation. MERRA-2 precipitation data distributed similarly to the modeled and satellite rainfall fields but, presented significantly lower magnitudes due to the coarser resolution.

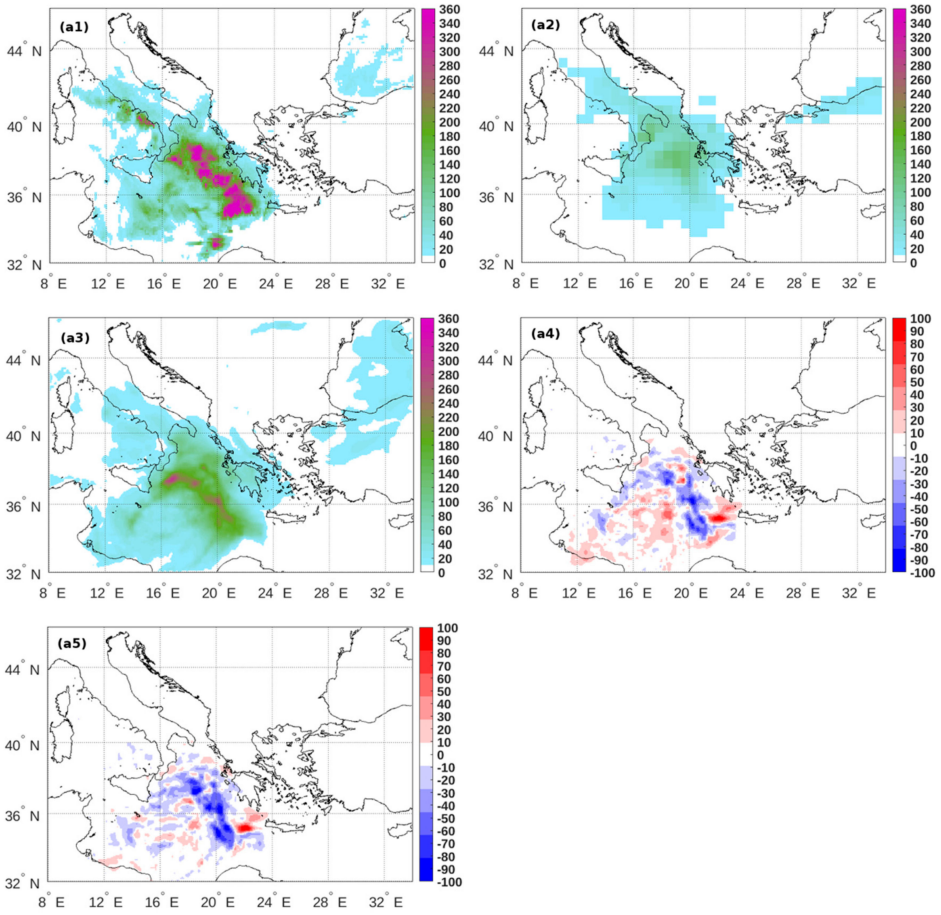


Figure 15. (**a1**) Accumulated precipitation field in millimeters from IMERG satellite data, (**a2**) accumulated precipitation field in millimeters from MERRA-2 reanalysis (**a3**) accumulated precipitation in millimeters field from RTG-sst run (**a4**) differences in accumulated precipitation fields between NEMO-sst and RTG-sst, and (**a5**) differences in accumulated precipitation fields between OSTIA-sst and RTG-sst, for cyclone Trixi.

For cyclone Numa, maximum rainfall values were distinctly placed on the east coast of Italy (Gulf of Taranto) in a structure that also implied the position of the cyclone center (Figure 16). Moreover, rain

bands in a radius of approximately five degrees were also illustrated in the southern Mediterranean Sea. Modeled, satellite-derived and MERRA-2 reanalysis rain amounts followed similar patterns in most of the affected areas. Overall, an underprediction of model results with respect to satellite accumulated rain fields occurred. This also concerns the rain maxima that emerged in the satellite estimates that were not detectable in the simulations. However, these take place in limited spatial scales. Between the different simulations, minimal differences were presented, noting small deviations between the SST fields. MERRA-2 maximum values could be mainly found in the mainland of Greece and Italy in comparison with that of modeled and remote sensing that were also observed in the Adriatic Sea. The same result was evident in a relevant modeling study of cyclone Numa, also supported by radar data [37].

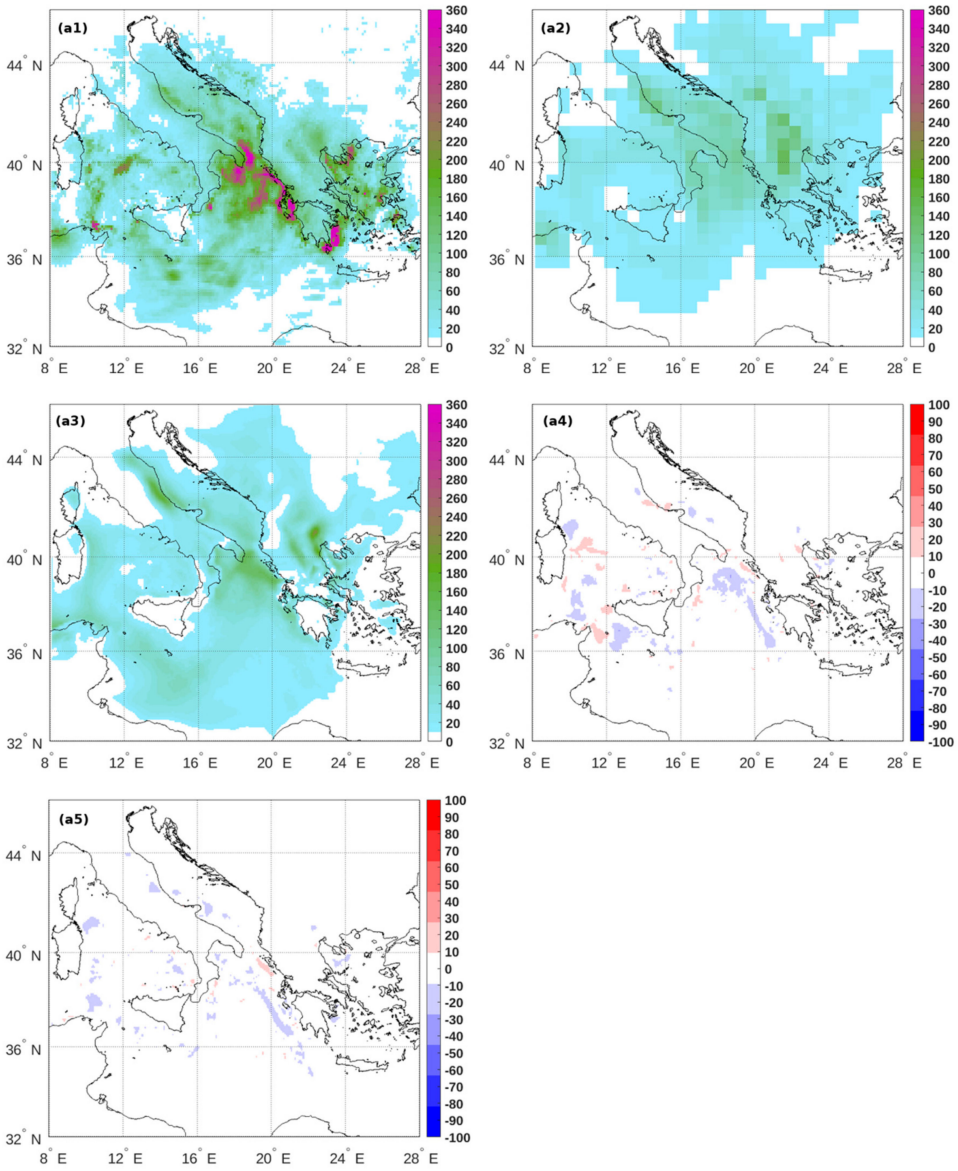


Figure 16. (**a1**) Accumulated precipitation fields in millimeters from IMERG satellite data, (**a2**) accumulated precipitation field in millimeters from MERRA-2 reanalysis, (**a3**) accumulated precipitation field in millimeters from RTG-sst run (**a4**) differences in accumulated precipitation fields between NEMO-sst and RTG-sst, and (**a5**) differences in accumulated precipitation fields between OSTIA-sst and RTG-sst, for cyclone Numa.

Concerning cyclone Zorbas, the accumulated precipitation fields derived from the satellite estimates tended to extreme rainfall values in the South Mediterranean (Figure 17). Unfortunately, due to the area where the maxima appear, verification with ground observations was not feasible. Cumulatively, remote sensing, simulated and reanalysis fields from MERRA-2 correlated well spatially. Maximum values were also located in the same area. OSTIA-sst and NEMO-sst rain fields were considerably lower, as compared to the RTG. This was the result of the higher initial SST fields in RTG-sst simulation, as compared to the OSTIA-sst and NEMO-sst runs. The warmer sea surfaces provided more energy and water vapor to the system, intensifying it and creating conditions with increased rainfall rates.

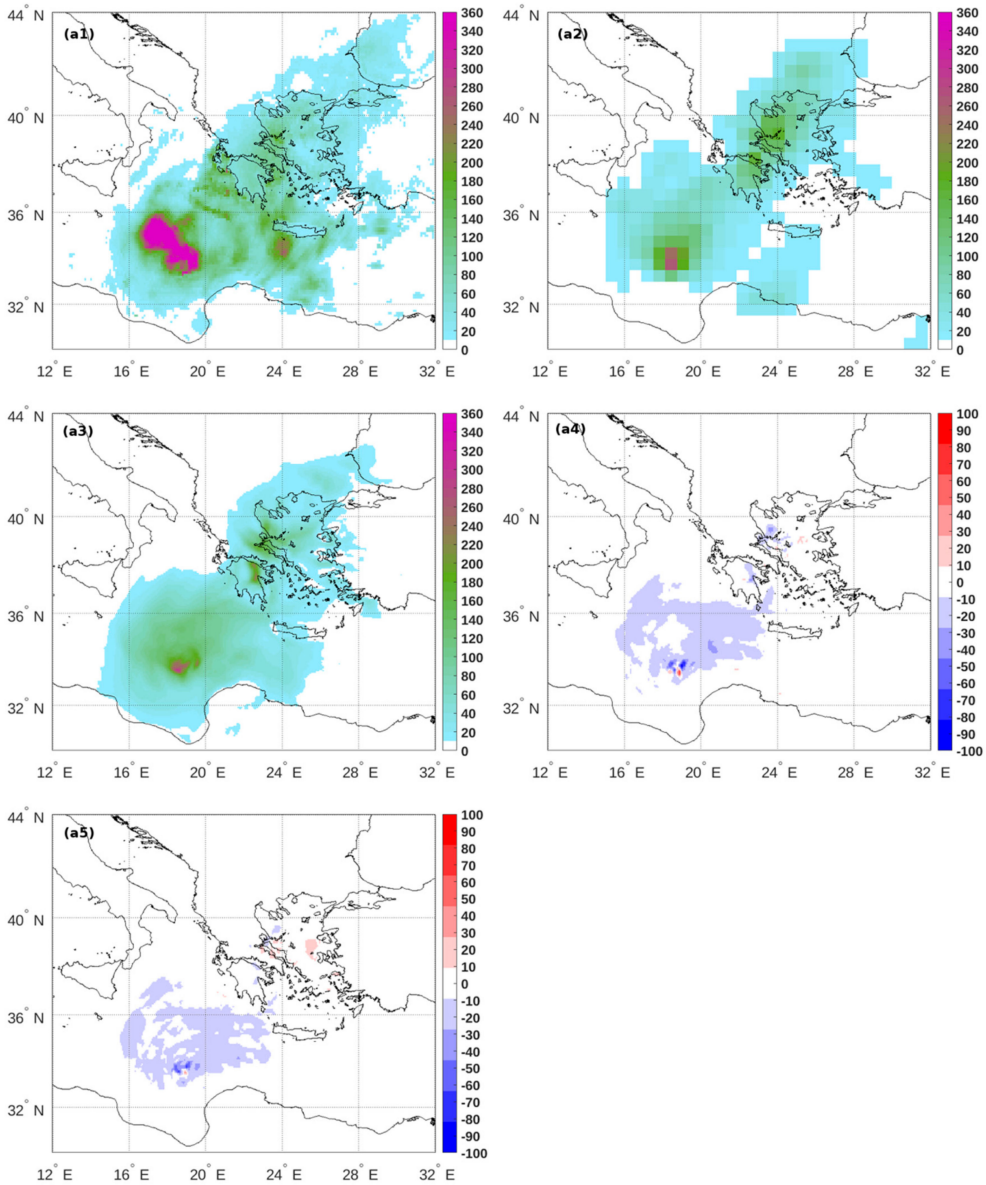


Figure 17. (**a1**) Accumulated precipitation fields in millimeter from IMERG satellite data, (**a2**) accumulated precipitation field in millimeters from MERRA-2 reanalysis, (**a3**) accumulated precipitation field in millimeters from RTG-sst run (**a4**) differences in accumulated precipitation fields between NEMO-sst and RTG-sst, and (**a5**) differences in accumulated precipitation fields between OSTIA-sst and RTG-sst, for cyclone Zorbas.

4. Summary and Conclusions

In this study, an analysis of the impact of the SST on the lifecycle of Mediterranean cyclones with tropical-like characteristics was attempted following different methodologies. A coupled atmospheric/wave–ocean modeling system was used to investigate the influence of the SST on the formation and evolution of cyclonic events.

The importance of the water surface temperature in the creation, evolution, and intensity of Mediterranean cyclones has received a lot of attention in previous studies. These were mainly focused on the implementation of uniform warm or cold SST anomalies [4,8,59]. The current work approached this issue with the use of static and dynamic SST fields from various sources in the simulation of three cyclonic events. These concern modeled and operational daily and hourly analysis SST results enriched with remote sensing data. Precisely, the RTG, OSTIA, and NEMO SST products with broad implementation were used. Therefore, it is arguable that spatiotemporal deviations in the SST forcing seem to mainly contribute to the differences between the model results as there are no significant differences in the maximum/minimum SST values. All numerical experiments performed with the different SST inputs seemed to be adequate for the modeling of the cyclonic systems. This was also supported by the comparison with remote sensing estimates of wind, wave, and precipitation. The utilization of different SSTs did not seem to affect the forecasting skill drastically. Maximum wind speed variations and spatial rain distributions were sufficiently described.

SST deviations did not lead to considerable deviations in model results regarding cyclone tracks, intensities, and wind speed. The most noticeable differences were found in the surface pressure in the simulations of cyclone Trixi and Zorbas. In contrast, the use of alternative SST products in the simulation of cyclone Numa did not seem to provide different model results. This could be attributed to the distinct dynamics and characteristics of this cyclone with a strong relation to large scale processes in the upper atmosphere and baroclinic instability rather than the influence of the SST dissimilarities.

The analysis of the different model results did not imply significant differences in the evolution of the structural characteristics of the cyclones. The RTG-sst simulations resulted in more intensified tropical-type properties, as shown in the peaks of cyclones Zorbas and Trixi. Both were characterized by a deep-warm core structure. However, cyclone Trixi for most of its lifetime, remained in an extra-tropical stage presenting tropical characteristics for a short period. Conversely, cyclone Numa was limited to an extra-tropical type storm without denoting significant differences between the different simulations.

Considerable deviations emerged in the resulted heat fluxes. RTG products, in general, corresponded to warmer seas as compared to OSTIA and NEMO. As a result, both sensible and latent heat fluxes from RTG-sst simulations exceeded the ones from OSTIA-sst and NEMO-sst ones. Apparently, the absence of diurnal variation, including cooling effects, in the RTG SST led to enhanced upward heat fluxes. Nevertheless, cold SST anomalies from the storm passage were evident in daily temporal intervals. This was indicatively shown in the case of cyclone Zorbas.

The most important differences were found in precipitation exhibiting spatial and intensity differences. The warmer sea surfaces presented in the RTG products provided energy and water vapor to the cyclonic systems and favored conditions with increased rainfall rates. On the other hand, model precipitation rates were lower as compared to satellite products.

Overall, SST conditions play a crucial role in the development and evolution of cyclones in the Mediterranean Sea. Even the employment of widely used products is shown to result in different outcomes and this point should be taken into consideration in forecasting and early warning systems.

Author Contributions: C.S. performed computations, analysis, and wrote the manuscript. P.P. aided in analysis and writing and C.T. contributed to suggestions. G.K. contributed to the final reading and suggestions. All authors have read and agreed to the published version of the manuscript.

Funding: This research was co-funded by the European Union (ESF) and Greek national funds through the Operational Program "Human Resources Development, Education and Lifelong Learning", project title "Study of Extreme Environmental with Numerical Weather Prediction Models and Stochastic Processes" (project code: MIS 5007050).

Acknowledgments: The research leading to these results has been co-funded by the European Commission under the H2020 Research Infrastructures contract no. 675121 (project VI-SEEM), upon computational time. Platon Patlakas would like to acknowledge Robert Hart for his guidance in the creation of Phase Diagrams. Authors would like to acknowledge all data providers. This study has been conducted using E.U. Copernicus Marine Service Information (http://marine.copernicus.eu/), precisely the OSTIA and NEMO SST data. Data for the buoy was available from the European Marine Observation and Data Network (https://www.emodnet-physics.eu). Blended Sea Winds data, JASON2, and JASON3 satellite altimetry data were available from the National Centers for Environmental Information (https://www.ncdc.noaa.gov). Remote sensing precipitation estimates and MERRA-2 reanalysis data were provided by the National Aeronautics and Space Administration (https://pmm.nasa.gov). The authors would like also to thank the four anonymous reviewers for their comments that improved the manuscript.

Conflicts of Interest: The authors declare no conflict of interest.

Appendix A

The structural evolution of the cyclones can be analyzed in terms of the thermal core structure and thickness asymmetry. To describe these features during the lifetime of a cyclonic system, the phase diagrams proposed by Hart [28] were implemented. The construction of the diagrams was based on parameter B, which stands for the thermal symmetry and the parameters $-\left|V_T^U\right|$ and $-\left|V_T^L\right|$ that represent the upper and lower thermal wind, respectively. Namely, the thermal symmetry was defined as $B = h\left(\overline{\Phi_{600hPa} - \Phi_{900hPa}}\big|_R - \overline{\Phi_{600hPa} - \Phi_{900hPa}}\big|_L\right)$, with h an integer equal to 1 for the North Hemisphere, Φ the geopotential height while R and L indicate the right and left sides related to the storm motion.

$B \gg 0$, refers to thermally asymmetric or frontal nature cyclones with/and extratropical type, matured, or conventionally intensified. Values of $\cong 0$, denote matured tropical cyclones, with non-frontal nature or thermally symmetric. A threshold between the tropical and extratropical type was set close to 10 m.

The thermal winds were defined as: $-\left|V_T^L\right| = \frac{\partial(\Delta\Phi)}{\partial(lnp)}\big|_{900hPa}^{600hPa}$ for the upper thermal wind between 300–600 hPa focusing on the middle/upper atmosphere and $-\left|V_T^U\right| = \frac{\partial(\Delta\Phi)}{\partial(lnp)}\big|_{600hPa}^{300hPa}$ for the lower thermal wind between the 600–900 hPa referring to the lower/middle atmosphere. Both expressions in positive values indicate a warm-core structure and a cold-structure otherwise.

References

1. Pytharoulis, I.; Craig, G.C.; Ballard, S.P. Study of the Hurricane-like Mediterranean cyclone of January 1995. *Phys. Chem. Earth Part B Hydrol. Ocean. Atmos.* **1999**, *24*, 627–632. [CrossRef]
2. Emanuel, K. Genesis and maintenance of "Mediterranean hurricanes". *Adv. Geosci.* **2005**, *2*, 217–220. [CrossRef]
3. Miglietta, M.M.; Mastrangelo, D.; Conte, D. Influence of physics parameterization schemes on the simulation of a tropical-like cyclone in the Mediterranean Sea. *Atmos. Res.* **2015**, *153*, 360–375. [CrossRef]
4. Miglietta, M.M.; Moscatello, A.; Conte, D.; Mannarini, G.; Lacorata, G.; Rotunno, R. Numerical analysis of a Mediterranean 'hurricane' over south-eastern Italy: Sensitivity experiments to sea surface temperature. *Atmos. Res.* **2011**, *101*, 412–426. [CrossRef]
5. Emanuel, K.A. An Air-Sea Interaction Theory for Tropical Cyclones. Part I: Steady-State Maintenance. *J. Atmos. Sci.* **1986**, *43*, 585–605. [CrossRef]
6. Miglietta, M.M.; Rotunno, R. Development mechanisms for Mediterranean tropical-like cyclones (medicanes). *Q. J. R. Meteorol. Soc.* **2019**, *145*, 1444–1460. [CrossRef]
7. Shi, Q.; Bourassa, M.A. Coupling Ocean Currents and Waves with Wind Stress over the Gulf Stream. *Remote Sens.* **2019**, *11*, 1476. [CrossRef]
8. Pytharoulis, I. Analysis of a Mediterranean tropical-like cyclone and its sensitivity to the sea surface temperatures. *Atmos. Res.* **2018**, *208*, 167–179. [CrossRef]

9. Lellouche, J.M.; Greiner, E.; Le Galloudec, O.; Garric, G.; Regnier, C.; Drevillon, M.; Benkiran, M.; Testut, C.E.; Bourdalle-Badie, R.; Gasparin, F.; et al. Recent updates to the Copernicus Marine Service global ocean monitoring and forecasting real-time 1/12° high-resolution system. *Ocean Sci.* **2018**, *14*, 1093–1126. [CrossRef]
10. Donlon, C.J.; Martin, M.; Stark, J.; Roberts-Jones, J.; Fiedler, E.; Wimmer, W. The Operational Sea Surface Temperature and Sea Ice Analysis (OSTIA) system. *Remote Sens. Environ.* **2012**, *116*, 140–158. [CrossRef]
11. Warner, J.C.; Armstrong, B.; He, R.; Zambon, J.B. Development of a Coupled Ocean–Atmosphere–Wave–Sediment Transport (COAWST) Modeling System. *Ocean Model.* **2010**, *35*, 230–244. [CrossRef]
12. Georg, L. Newsletter No. 154—Winter 2017/18. 2018.
13. Doyle, J.D.; Hodur, R.M.; Chen, S.U.E.; Jin, Y.I.; Moskaitis, J.R.; Wang, S.; Hendricks, E.A.; Jin, H.A.O.; Smith, T.A. Tropical Cyclone Prediction Using COAMPS-TC. *Oceanography* **2014**, *27*, 104–115. [CrossRef]
14. Cotton, W.R.; Pielke, R.A., Sr.; Walko, R.L.; Liston, G.E.; Tremback, C.J.; Jiang, H.; McAnelly, R.L.; Harrington, J.Y.; Nicholls, M.E.; Carrio, G.G.; et al. RAMS 2001: Current status and future directions. *Meteorol. Atmos. Phys.* **2003**, *82*, 5–29. [CrossRef]
15. Kallos, G.; Solomos, S.; Kushta, J.; Mitsakou, C.; Spyrou, C.; Bartsotas, N.; Kalogeri, C. Natural and anthropogenic aerosols in the Eastern Mediterranean and Middle East: Possible impacts. *Sci. Total Environ.* **2014**, *488–489*, 389–397. [CrossRef] [PubMed]
16. Solomos, S.; Kallos, G.; Kushta, J.; Astitha, M.; Tremback, C.; Nenes, A.; Levin, Z. An integrated modeling study on the effects of mineral dust and sea salt particles on clouds and precipitation. *Atmos. Chem. Phys.* **2011**, *11*, 873–892. [CrossRef]
17. Patlakas, P.; Stathopoulos, C.; Flocas, H.; Kalogeri, C.; Kallos, G. Regional Climatic Features of the Arabian Peninsula. *Atmosphere* **2019**, *10*, 220. [CrossRef]
18. Gong, S.L. A parameterization of sea-salt aerosol source function for sub- and super-micron particles. *Glob. Biogeochem. Cycles* **2003**, *17*. [CrossRef]
19. Iacono, M.J.; Delamere, J.S.; Mlawer, E.J.; Shephard, M.W.; Clough, S.A.; Collins, W.D. Radiative forcing by long-lived greenhouse gases: Calculations with the AER radiative transfer models. *J. Geophys. Res. Atmos.* **2008**, *113*. [CrossRef]
20. Fountoukis, C.; Nenes, A. Continued development of a cloud droplet formation parameterization for global climate models. *J. Geophys. Res. Atmos.* **2005**, *110*. [CrossRef]
21. Group, T.W. The WAM Model—A Third Generation Ocean Wave Prediction Model. *J. Phys. Oceanogr.* **1988**, *18*, 1775–1810. [CrossRef]
22. Bidlot, J.; Janssen, P. *Unresolved Bathymetry, Neutral Winds and New Stress Tables in WAM*; ECMWF: Reading, UK, 2003.
23. Valcke, S. The OASIS3 coupler: A European climate modelling community software. *Geosci. Model. Dev.* **2013**, *6*, 373–388. [CrossRef]
24. Taylor, P.K.; Yelland, M.J. The Dependence of Sea Surface Roughness on the Height and Steepness of the Waves. *J. Phys. Oceanogr.* **2001**, *31*, 572–590. [CrossRef]
25. Drennan, W.M.; Taylor, P.K.; Yelland, M.J. Parameterizing the Sea Surface Roughness. *J. Phys. Oceanogr.* **2005**, *35*, 835–848. [CrossRef]
26. Olabarrieta, M.; Warner, J.C.; Armstrong, B.N.; Zambon, J.B.; He, R. Ocean-atmosphere dynamics during Hurricane Ida and Nor'Ida: An application of the coupled ocean-atmosphere-wave-sediment transport (COAWST) modeling system. *Ocean Model.* **2012**, *43–44*, 112–137. [CrossRef]
27. Ricchi, A.; Miglietta, M.M.; Barbariol, F.; Benetazzo, A.; Bergamasco, A.; Bonaldo, D.; Cassardo, C.; Falcieri, F.M.; Modugno, G.; Russo, A.; et al. Sensitivity of a Mediterranean Tropical-Like Cyclone to Different Model Configurations and Coupling Strategies. *Atmosphere* **2017**, *8*, 92. [CrossRef]
28. Hart, R.E. A Cyclone Phase Space Derived from Thermal Wind and Thermal Asymmetry. *Mont. Weather Rev.* **2003**, *131*, 585–616. [CrossRef]
29. Astitha, M.; Kallos, G. Gas-phase and aerosol chemistry interactions in South Europe and the Mediterranean region. *Environ. Fluid Mech.* **2009**, *9*, 3–22. [CrossRef]
30. Thiébaux, J.; Rogers, E.; Wang, W.; Katz, B. A New High-Resolution Blended Real-Time Global Sea Surface Temperature Analysis. *Bull. Am. Meteorol. Soc.* **2003**, *84*, 645–656. [CrossRef]
31. Borde, R.; Carranza, M.; Hautecoeur, O.; Barbieux, K. Winds of Change for Future Operational AMV at EUMETSAT. *Remote Sens.* **2019**, *11*, 2111. [CrossRef]

32. Madec, G. NEMO Ocean Engine. Note du Pôle de Modélisation. In *ISSN*; Institut Pierre-Simon Laplace (IPSL): Paris, France, 2008; Volume 27, pp. 1288–1619.
33. Becker, J.J.; Sandwell, D.T.; Smith, W.H.F.; Braud, J.; Binder, B.; Depner, J.; Fabre, D.; Factor, J.; Ingalls, S.; Kim, S.H.; et al. Global Bathymetry and Elevation Data at 30 Arc Seconds Resolution: SRTM30_PLUS. *Mar. Geod.* **2009**, *32*, 355–371. [CrossRef]
34. Amante, C.; Eakins, B.W. *ETOPO1 Global Relief Model Converted to PanMap Layer Format*; PANGAEA: Boulder, CO, USA, 2009. [CrossRef]
35. Gasparin, F.; Greiner, E.; Lellouche, J.-M.; Legalloudec, O.; Garric, G.; Drillet, Y.; Bourdallé-Badie, R.; Traon, P.-Y.L.; Rémy, E.; Drévillon, M. A large-scale view of oceanic variability from 2007 to 2015 in the global high resolution monitoring and forecasting system at Mercator Océan. *J. Mar. Syst.* **2018**, *187*, 260–276. [CrossRef]
36. Nastos, P.T.; Karavana Papadimou, K.; Matsangouras, I.T. Mediterranean tropical-like cyclones: Impacts and composite daily means and anomalies of synoptic patterns. *Atmos. Res.* **2018**, *208*, 156–166. [CrossRef]
37. Marra, C.A.; Federico, S.; Montopoli, M.; Avolio, E.; Baldini, L.; Casella, D.; D'Adderio, P.L.; Dietrich, S.; Sanò, P.; Torcasio, C.R.; et al. The Precipitation Structure of the Mediterranean Tropical-Like Cyclone Numa: Analysis of GPM Observations and Numerical Weather Prediction Model Simulations. *Remote Sens.* **2019**, *11*, 1690. [CrossRef]
38. Zhang, H.-M.; Bates, J.J.; Reynolds, R.W. Assessment of composite global sampling: Sea surface wind speed. *Geophys. Res. Lett.* **2006**, *33*. [CrossRef]
39. Peng, G.; Zhang, H.-M.; Frank, H.P.; Bidlot, J.-R.; Higaki, M.; Stevens, S.; Hankins, W.R. Evaluation of Various Surface Wind Products with OceanSITES Buoy Measurements. *Weather Forecast.* **2013**, *28*, 1281–1303. [CrossRef]
40. Schmidt, K.M.; Swart, S.; Reason, C.; Nicholson, S.-A. Evaluation of Satellite and Reanalysis Wind Products with In Situ Wave Glider Wind Observations in the Southern Ocean. *J. Atmos. Ocean. Technol.* **2017**, *34*, 2551–2568. [CrossRef]
41. Zecchetto, S.; De Biasio, F.; Music, S.; Nickovic, S.; Pierdicca, N. Intercomparison of satellite observations and atmospheric model simulations of a meso-scale cyclone in the Mediterranean Sea. *Can. J. Remote Sens.* **2002**, *28*, 413–423. [CrossRef]
42. Hong, Y.; Hsu, K.-L.; Sorooshian, S.; Gao, X. Precipitation Estimation from Remotely Sensed Imagery Using an Artificial Neural Network Cloud Classification System. *J. Appl. Meteorol.* **2004**, *43*, 1834–1853. [CrossRef]
43. Huffman, G.J.; Bolvin, D.T.; Nelkin, E.J.; Wolff, D.B.; Adler, R.F.; Gu, G.; Hong, Y.; Bowman, K.P.; Stocker, E.F. The TRMM Multisatellite Precipitation Analysis (TMPA): Quasi-Global, Multiyear, Combined-Sensor Precipitation Estimates at Fine Scales. *J. Hydrometeorol.* **2007**, *8*, 38–55. [CrossRef]
44. Tan, J.; Petersen, W.A.; Kirstetter, P.-E.; Tian, Y. Performance of IMERG as a Function of Spatiotemporal Scale. *J. Hydrometeorol.* **2017**, *18*, 307–319. [CrossRef]
45. Derin, Y.; Anagnostou, E.; Berne, A.; Borga, M.; Boudevillain, B.; Buytaert, W.; Chang, C.-H.; Chen, H.; Delrieu, G.; Hsu, Y.C.; et al. Evaluation of GPM-era Global Satellite Precipitation Products over Multiple Complex Terrain Regions. *Remote Sens.* **2019**, *11*, 2936. [CrossRef]
46. Collow, A.B.M.; Bosilovich, M.G.; Koster, R.D. Large-Scale Influences on Summertime Extreme Precipitation in the Northeastern United States. *J. Hydrometeorol.* **2016**, *17*, 3045–3061. [CrossRef] [PubMed]
47. Xu, F.; Guo, B.; Ye, B.; Ye, Q.; Chen, H.; Ju, X.; Guo, J.; Wang, Z. Systematical Evaluation of GPM IMERG and TRMM 3B42V7 Precipitation Products in the Huang-Huai-Hai Plain, China. *Remote Sens.* **2019**, *11*, 697. [CrossRef]
48. Ramsauer, T.; Weiß, T.; Marzahn, P. Comparison of the GPM IMERG Final Precipitation Product to RADOLAN Weather Radar Data over the Topographically and Climatically Diverse Germany. *Remote Sens.* **2018**, *10*, 2029. [CrossRef]
49. Kirstetter, P.-E. Evaluation of diurnal variation of GPM IMERG-derived summer precipitation over the contiguous US using MRMS data. *Q. J. R. Meteorol. Soc.* **2018**, *144*, 270–281. [CrossRef]
50. Abdalla, S.; Janssen, P.A.E.M.; Bidlot, J.-R. Jason-2 OGDR Wind and Wave Products: Monitoring, Validation and Assimilation. *Mar. Geod.* **2010**, *33*, 239–255. [CrossRef]
51. Bhowmick, S.A.; Sharma, R.; Babu, K.N.; Shukla, A.K.; Kumar, R.; Venkatesan, R.; Gairola, R.M.; Bonnefond, P.; Picot, N. Validation of SWH and SSHA from SARAL/AltiKa Using Jason-2 and In-Situ Observations. *Mar. Geod.* **2015**, *38*, 193–205. [CrossRef]

52. Gelaro, R.; McCarty, W.; Suárez, M.J.; Todling, R.; Molod, A.; Takacs, L.; Randles, C.A.; Darmenov, A.; Bosilovich, M.G.; Reichle, R.; et al. The Modern-Era Retrospective Analysis for Research and Applications, Version 2 (MERRA-2). *J. Clim.* **2017**, *30*, 5419–5454. [CrossRef]
53. Reichle, R.H.; Liu, Q.; Koster, R.D.; Draper, C.S.; Mahanama, S.P.P.; Partyka, G.S. Land Surface Precipitation in MERRA-2. *J. Clim.* **2017**, *30*, 1643–1664. [CrossRef]
54. Lin, I.-I.; Liu, W.T.; Wu, C.-C.; Chiang, J.C.H.; Sui, C.-H. Satellite observations of modulation of surface winds by typhoon-induced upper ocean cooling. *Geophys. Res. Lett.* **2003**, *30*. [CrossRef]
55. Bender, M.A.; Ginis, I. Real-Case Simulations of Hurricane–Ocean Interaction Using A High-Resolution Coupled Model: Effects on Hurricane Intensity. *Mon. Weather Rev.* **2000**, *128*, 917–946. [CrossRef]
56. Schade, L.R.; Emanuel, K.A. The Ocean's Effect on the Intensity of Tropical Cyclones: Results from a Simple Coupled Atmosphere–Ocean Model. *J. Atmos. Sci.* **1999**, *56*, 642–651. [CrossRef]
57. Perrie, W.; Ren, X.; Zhang, W.; Long, Z. Simulation of extratropical Hurricane Gustav using a coupled atmosphere-ocean-sea spray model. *Geophys. Res. Lett.* **2004**, *31*. [CrossRef]
58. Wilks, D.S. (Ed.) Chapter 8—Forecast Verification. In *International Geophysics*; Academic Press: Cambridge, MA, USA, 2011; Volume 100, pp. 301–394.
59. Noyelle, R.; Ulbrich, U.; Becker, N.; Meredith, E.P. Assessing the impact of sea surface temperatures on a simulated medicane using ensemble simulations. *Nat. Hazards Earth Syst. Sci.* **2019**, *19*, 941–955. [CrossRef]



© 2020 by the authors. Licensee MDPI, Basel, Switzerland. This article is an open access article distributed under the terms and conditions of the Creative Commons Attribution (CC BY) license (http://creativecommons.org/licenses/by/4.0/).